Author/s:
Liu, Z;Qiao, R;Feng, D;Zhou, J;Di, H;Bai, Y;Liu, D;Shi, N;Huang, W-H;Yeh, M-H;Pao, C-W;Hu, Z;Yang, G;Lin, Y;Luo, Z;Ran, R;Zhou, W;Zhu, Y;Shao, Z

Title:
Strategic atomic trapping at heterointerfaces for protonic ceramic cells.

Date:
2025-11-24

Citation:
Liu, Z., Qiao, R., Feng, D., Zhou, J., Di, H., Bai, Y., Liu, D., Shi, N., Huang, W. -H., Yeh, M. -H., Pao, C. -W., Hu, Z., Yang, G., Lin, Y., Luo, Z., Ran, R., Zhou, W., Zhu, Y. & Shao, Z. (2025). Strategic atomic trapping at heterointerfaces for protonic ceramic cells.. Nat Commun, 16 (1), pp.10405-. https://doi.org/10.1038/s41467-025-65386-8.

Persistent Link:
https://hdl.handle.net/11343/367956

nature communications

Article

https://doi.org/10.1038/s41467-025-65386-8

Strategic atomic trapping at heterointerfaces for protonic ceramic cells

Received: 28 May 2025

Accepted: 8 October 2025

Zuoqing Liu[1], Ruixi Qiao[2], Desheng Feng[3], Jin Zhou[4], Haosong Di[1], Yuesheng Bai[1], Dongliang Liu[1], Nai Shi[5], Wei-Hsiang Huang[6,7], Min-Hsin Yeh[7,8], Chih-Wen Pao[6], Zhiwei Hu[9], Guangming Yang[1] ✉, Yuxiao Lin[10] ✉, Zhixin Luo[5], Ran Ran[1], Wei Zhou[1], Yinlong Zhu[2] & Zongping Shao[5] ✉

Engineering dynamic heterointerfaces with atomic precision is critical for unlocking the full potential of reversible protonic ceramic electrochemical cells in sustainable energy conversion, while minimizing precious metal use in composite electrodes. Here, we introduce an atomic trapping strategy that restructures the interfacial chemistry of $Ba_{0.5}Sr_{0.5}Co_{0.8}Fe_{0.2}O_{3-\delta}$ perovskite and Ru@$CeO_{2-\delta}$ fluorite heteroelectrodes, achieving catalytic synergy through manipulating Ru coordination environment. A scalable co-sintering protocol induces thermodynamically driven Ru migration from the CeO_2 lattice into the perovskite matrix, creating coupled interfaces. This optimizes interfacial electron redistribution, generates interfacial oxygen vacancies, and improves triple conductivity and hydration kinetics. The electrode with low Ru loading exhibits bifunctionality, delivering a peak power density of 1.51 W cm^{-2} and an electrolysis current density of −2.21 A cm^{-2} at 650 °C. It demonstrates notable durability with minimal degradation (0.09 mV h^{-1}) over 400 h at 600 °C, providing a universal strategy for next-generation solid-state energy devices.

The pursuit of robust electrochemical energy infrastructures has propelled reversible protonic ceramic electrochemical cells (R-PCECs) into the spotlight, due to their specific ability to switch reversibly between fuel cell and electrolysis modes with high energy efficiency at intermediate temperatures (400–600 °C)[1–4]. These devices hold great promise for bridging renewable electricity with storable chemical fuels—producing green hydrogen from intermittent solar and wind energy, while efficiently reconverting it to electrical power during peak grid demand[5,6]. The wide-spread applications of this technology require the development of efficient electrode with high activity, durability and cost effectiveness. Noble metal oxides like RuO_2 are highly active for catalyzing oxygen reduction reaction (ORR) and oxygen evolution reaction (OER), while their high price inhibits the use in large amount[7,8]. In addition, a fundamental contradiction remains that inhibits the development of robust R-PCECs, i.e., the very interfacial architectures that enable multifunctionality also inherently drive operational degradation[3,9]. State-of-the-art air electrodes, responsible for facilitating both ORR and OER during bidirectional operation, suffer significant performance losses due to interfacial detachment—a mechanically driven failure mode that accelerates catalytic

---

[1]State Key Laboratory of Materials-Oriented Chemical Engineering, College of Chemical Engineering, Nanjing Tech University, Nanjing, China. [2]Institute for Frontier Science, Nanjing University of Aeronautics and Astronautics, Nanjing, China. [3]Department of Chemical Engineering, University of Melbourne, Melbourne, Australia. [4]Zhejiang Institute of Photoelectronics & Zhejiang Institute for Advanced Light Source, Zhejiang Normal University, Jinhua, Zhejiang, China. [5]WA School of Mines: Minerals, Energy and Chemical Engineering (WASM-MECE), Curtin University, Perth, WA, Australia. [6]National Synchrotron Radiation Research Center, Hsinchu, Taiwan. [7]Sustainable Electrochemical Energy Development (SEED) Center, National Taiwan University of Science and Technology, Taipei, Taiwan. [8]Department of Chemical Engineering, National Taiwan University of Science and Technology, Taipei, Taiwan. [9]Max-Planck-Institute for Chemical Physics of Solids, Dresden, Germany. [10]School of Physics and Electronic Engineering, Jiangsu Normal University, Xuzhou, China.
✉e-mail: ygm89525@njtech.edu.cn; linyuxiao@jsnu.edu.cn; zongping.shao@curtin.edu.au

deactivation and disrupts ionic conduction networks under prolonged operation[10,11]. Therefore, development of efficient electrode materials with minimized use of precious metal elements and re-enforced interface is crucial in the development of R-PCEC.

Precious metal-free perovskite oxides, such as $Ba_{0.5}Sr_{0.5}Co_{0.8}Fe_{0.2}O_{3-\delta}$ (BSCF), $PrBa_{0.5}Sr_{0.5}Co_{1.5}Fe_{0.5}O_{5+\delta}$ (PBSCF), $BaCo_{0.4}Fe_{0.4}Zr_{0.1}Y_{0.1}O_{3-\delta}$ (BCFZY), and $Ba_{0.875}Fe_{0.875}Zr_{0.125}O_{3-\delta}$ (BFZ), have dominated R-PCEC electrode designs, leveraging their high ionic conductivity and flexible oxygen non-stoichiometry[12–14]. Despite considerable progress, the performance and stability of R-PCECs remain insufficient for practical applications. This limitation primarily stems from weakly bonded heterogeneous structures at the interfaces between cell components, which hinder ionic and electronic conduction, leading to increased interfacial resistance at intermediate to low temperatures[9,15]. Nanocomposites have emerged as a useful air electrode for R-PCEC with improved proton conductivity and reduced thermal expansion, while they introduce internal interface issues inside the electrodes[16]. Interface engineering is then proposed, which presents a promising approach to enhance cell performance in terms of both activity and durability by optimizing the contact area, coupling interactions, charge distribution, and lattice structure at these critical interfaces[16,17].

Current interface engineering, ranging from chemical etching to nanocomposite interlayers, however, merely treats symptoms (e.g., contact resistance) rather than curing the root disease[3,9]. For example, roughening electrolyte surfaces through acid treatment or incorporating phase-separated composite interlayers has been shown to improve electrode/electrolyte interactions, reducing interfacial resistance and improving electrochemical performance[3]. While recent advances in interface tailoring offer glimpses of hope, but demand energy-intensive processes incompatible with industrial scale-up[18–20]. More critically, the far greater design complexity arises from the internal interfaces within composite electrode matrices, where the synergistic interactions between the multiple phases at the interface dictate overall electrochemical activity and stability[21]. This emphasizes the deterministic role of internal heterointerfaces. Recent advances have primarily addressed simpler electrode/electrolyte interfaces, leaving the vastly more complex internal electrode architecture largely unoptimized, which is a critical gap that fundamentally limits R-PCEC development.

Here, we report an active atom-scale interface engineering strategy through manipulating the Ru migration that greatly increases the activity and durability for both ORR and OER in R-PCECs while realizing minimal use of the precious metal element. We first doped a minor amount of Ru into the lattice of CeO_2 (RC), and then composited it with BSCF perovskite to form a composite electrode. A subsequent thermal processing then deliberately triggered controlled Ru migration, and selective capture of migrating Ru atoms from the RC phase by BSCF was happened (Fig. 1a, b), which facilitated the formation of covalent metal-oxygen bridges at the rich interfaces between the two phases, thereby achieving interfacial charge redistribution, generating rich interfacial oxygen vacancies, and imparting favorable triple conductivity and hydration elasticity (Fig. 1c, d). Leveraging these synergistic effects, our R-PCECs demonstrated absolute advantages in bifunctionality, achieving an area-specific resistance of 0.08 Ω cm^2 at 600 °C, with negligible decay in reversible variable current density cycling (96 cycles) and thermal cycling tests. More importantly, we interpreted these macroscopic triumphs through experiments and theoretical analysis, establishing a universal interface regulation rule, providing a scalable and viable solution for advancing R-PCEC technology.

Results

Evaluation of heterogeneous structures

Composite electrodes often show competitive activity for ORR in protonic ceramic cells due to the potential of synergy between the different phases. $Sm_{0.2}Ce_{0.8}O_{2-\delta}$, due to its high oxygen ion conductivity, is widely used in composite electrodes. Here, a Ru-doped CeO_2 catalyst (Ru@$CeO_{2-\delta}$, denoted as RC) as a second phase for composite electrode is synthesized through a co-precipitation method followed by calcination at 800 °C for 2 h. Rietveld refinement of X-ray diffraction (XRD) data confirms the pure-phase fluorite cubic structure, without any detectable RuO_2 peaks (Fig. 2a and Supplementary Fig. 1), indicating the successful incorporation of Ru into the fluorite phase[22]. The refined XRD data reveal that the RC catalyst has an Fm-3m space group, with lattice contraction (a = 5.4085 Å vs. 5.4110 Å for pristine CeO_2), indicating that Ru atoms are successfully introduced into the bulk phase (Δr = 0.08 Å) (Supplementary Fig. 2 and Supplementary Table 1)[23]. This lattice strain facilitates oxygen vacancy formation, as evidenced by Raman spectroscopy (Supplementary Fig. 3)[24]. Extended X-ray absorption fine structure (EXAFS) analysis (Fig. 2b) and atomic-resolution High-angle annular dark-field scanning transmission electron microscopy (HAADF-STEM) (Fig. 2c) reveal the coordination environment of Ru. The Fourier-transformed (FT) EXAFS spectra exhibit a dominant scattering peak at 1.5 Å, attributed to Ru-O coordination with an average coordination number of 3.9 (Supplementary Table 2), while no discernible Ru-Ru scattering contributions observed at 2.4 Å (Supplementary Fig. 4)[25]. These structural features, corroborated by HAADF-STEM and energy-dispersive X-ray spectroscopy (EDS) elemental mapping results (Fig. 2d), conclusively confirm the atomic dispersion of Ru species within the CeO_2 matrix.

We then combine RC with BSCF to form a composite electrode. The optimized BSCF: RC (70: 30 wt%; denoted as BSCF-RC30) composite preserves dual-phase integrity, as verified by Rietveld quantification (69.68 wt% perovskite, 30.32 wt% fluorite) (Fig. 2e and Supplementary Fig. 5)[26]. This suggests that BSCF-RC30 both maintains the integrity of the individual components and potentially benefits from the synergistic effect between the two phases. Structural analysis further reveals minimal variation in perovskite lattice parameters across BSCF, BSCF-C30 (Ru-free BSCF and CeO_2 composite at a 70:30 mass ratio), and BSCF-RC30 (Supplementary Fig. 6), attributable to the negligible ionic radius mismatch between Ru^{4+} and host Co/Fe cations (Δr <0.03 Å). For the fluorite phase, BSCF-RC30 shows a pronounced lattice contraction (a = 5.4059 Å) relative to both BSCF-C30 (a = 5.4102 Å) and the RC catalyst (a = 5.4085 Å) (Supplementary Table 1). This additional shrinkage is attributed to charge-compensating oxygen vacancies generated during the trapping of Ru, which shortens the average Ce-O bond length, facilitating the lowering of the proton hopping barrier and enhancing bulk proton conduction[27]. In addition, high-temperature XRD (HT-XRD) analysis is conducted to evaluate the thermal stability of the RC and BSCF-RC30 catalysts. As shown in Supplementary Fig. 7, both catalysts exhibit phase stability up to 800 °C, while the typical shift of the diffraction peaks is related to the materials' thermal reduction. The lattice fringe spacings of 0.28 and 0.23 nm, corresponding to the (200) planes of the fluorite phase and the (111) planes of the cubic perovskite structure, respectively (Fig. 2f), are observed in STEM image. The strong contact and positive interactions between the two phases, as seen in STEM images, are expected to enhance electrode stability and improve ionic diffusion at the heterogeneous interface (Supplementary Fig. 8)[28]. Crucially, the spatial redistribution of Ru species during interface formation is quantitatively mapped through EDS elemental analysis (Fig. 2g). Remarkably, Ru atoms migrate from the fluorite phase into adjacent perovskite domains during the co-sintering[29]. This thermodynamically driven spontaneous migration trend persists at multiple independent interfaces (Supplementary Fig. 9), demonstrating the thermodynamic preference for Ru doping into the perovskite lattice.

Complementary spectroscopic investigations corroborate this spontaneous atomic trapping phenomenon and reveal the evolution of the coordination environment. Raman analysis identifies three critical signatures (Supplementary Fig. 10): (1) an

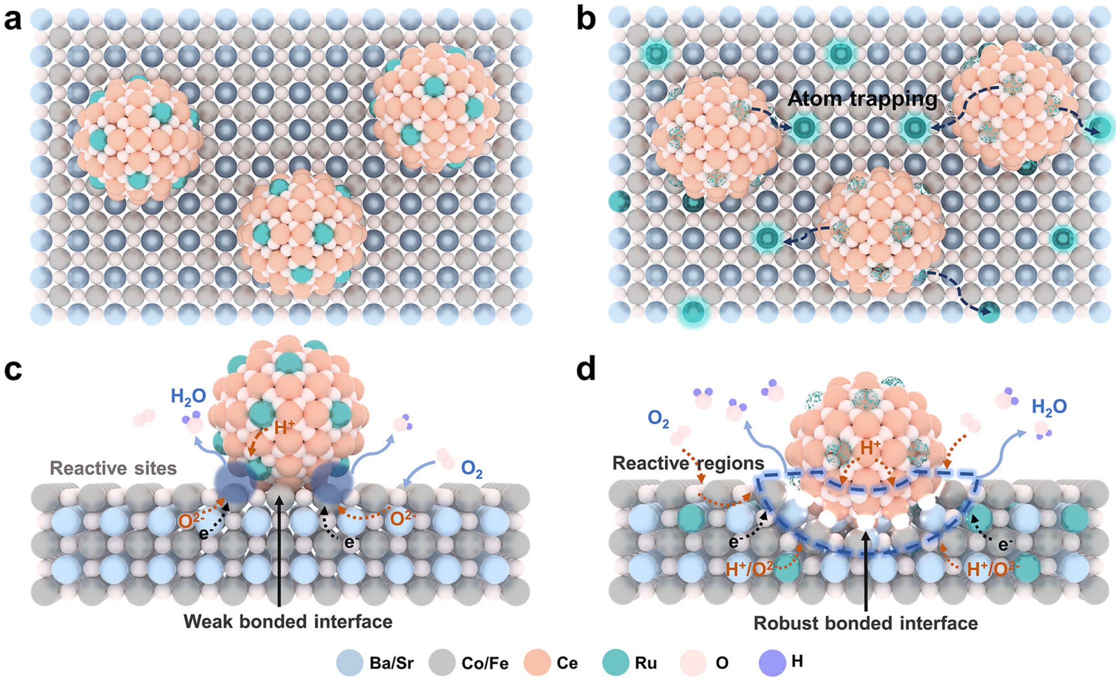

Fig. 1 | Schematic illustration of atom trapping. a, **b** Distribution of Ru element in heterogeneous catalyst before and after heat treatment. **c**, **d** Heterogeneous interface structure before and after atom trapping.

intrinsic F_{2g} mode at 465 cm^{-1}, (2) emergent peaks at 700/970 cm^{-1} (strain-induced Ru-O-Ce distortion in RC), and (3) complete disappearance of fluorite-associated signals in BSCF-RC30, which is crystallographic evidence of Ru depletion from CeO_2[22,30]. The FT EXAFS spectra of BSCF-RC30 display a predominant Ru-O peak (Fig. 2h), whereas the trapped Ru atoms transition from pseudo-tetrahedral geometry in CeO_2 ($CN_{Ru\text{-}O} = 3.9$) (Fig. 2b) to near-ideal octahedral coordination in BSCF ($CN_{Ru\text{-}O} = 6.3$) (Fig. 2i and Supplementary Table 2)[31]. The 61% increase in coordination number confirms the Ru integration into perovskite BO_6 frameworks, constituting a structural reorganization with significant kinetic implications.

Building on the aforementioned experimental characterizations, we further elucidate the underlying Ru migration mechanism at the interface through the climbing image nudged elastic band (CI-NEB) method[26,32]. The atomic coordinates for the optimized computational model were provided in Supplementary Data 1. For better comprehension, the interface before and after BSCF capture of Ru from RC are labelled as BSCF-RC and BSCFR-C (BSCFR: BSCF matrix after capture of Ru, C: pure CeO_2 phase), respectively. As illustrated in Fig. 2j, the Ru atom has a relatively low energy barrier of 1.14 eV to migrate from RC side to BSCF side, confirming the kinetic feasibility of the proposed Ru capture mechanism. Furthermore, Density functional theory (DFT) calculation also demonstrates that under the appearance of oxygen vacancy, the configuration with Ru atom on the surface layer (L1) is thermodynamically more stable ($\Delta E = -1.38$ eV) than that with Ru atom on the subsurface layer (L2), providing driving force for the continuous Ru migration to the BSCF phase (Fig. 2k and Supplementary Fig. 11). To validate the critical role of oxygen vacancy concentration in atomic trapping dynamics, we systematically investigate a counterexample of La_2NiO_4 (LN)-RC interface[33,34] with almost no oxygen vacancy, and reveals drastically different migration kinetics: Ru atom face a prohibitive energy barrier of 2.00 eV to migrate from RC side to LN side (Supplementary Fig. 12), higher than that in oxygen-deficient BSCFR-C. This is consistent with STEM energy-dispersive X-ray spectroscopy (STEM-EDS) mapping observation of Ru retainment in the CeO_2 matrix after the same heat treatment (Supplementary Fig. 13). Parallel DFT/CI-NEB simulations and STEM-EDS mapping of oxygen-vacancy-rich BSCF-RC interface versus the vacancy-poor LN-RC analogue demonstrate that lattice vacancies provide both a low-barrier migration channel and the deep B-site trap needed for irreversible Ru capture[30]. Crucially, this thermodynamically driven atomic trapping strategy through oxygen-vacancy pathways, thereby enhancing the triple conductivity and interfacial activity of the composite catalysts. This mechanism is fundamentally different from conventional reverse-trapping techniques, such as the acid-base extraction of alkaline-earth ions (e.g., Sr^{2+} removal by MoO_3), which rely primarily on surface effects[29].

Heterogeneous interfacial effect

To comprehensively resolve the electronic and structural interplay arising from thermodynamically driven Ru migration, we employed a synergistic multiscale characterization framework integrating X-ray absorption spectroscopy (XAS), Aberration-corrected TEM, Electron energy loss spectroscopy (EELS), Time-of-Flight Secondary Ion Mass spectroscopy (ToF-SIMS), and DFT calculations. This collective evidences delineate an activation mechanism at the BSCF-RC30 heterointerface, mediated by localized electron redistribution, vacancy-coupled oxygen dynamics, and proton transfer modulation.

X-ray absorption near-edge structure (XANES) analysis provides critical insights into the valence state evolution of heteroatoms during interfacial Ru migration. Notably, although Co and Fe K-edge spectra remain indistinguishable between pristine BSCF and post-treated BSCF-RC30 (Fig. 3a, b)[35,36], the Ru K-edge spectra reveal a striking valence shift from +3.34 in isolated RC nanoparticles (precursor phase) to +4.75 in the heterostructured system (Supplementary Fig. 14), which quantitatively demonstrates interfacial charge transfer during structural evolution (Fig. 3c)[7,23]. Also, this is confirmed by X-ray photoelectron spectroscopy (XPS) of Ru 3*p* orbitals for both RC and BSCF-RC30 (Supplementary Fig. 15). Notably, the retention of the near +4 state of the Ce ion (Supplementary Fig. 16) and unaltered Co/Fe coordination environments excludes bulk-phase compositional changes, pinpointing the interfacial region as the exclusive locus of electronic reconfiguration[37,38].

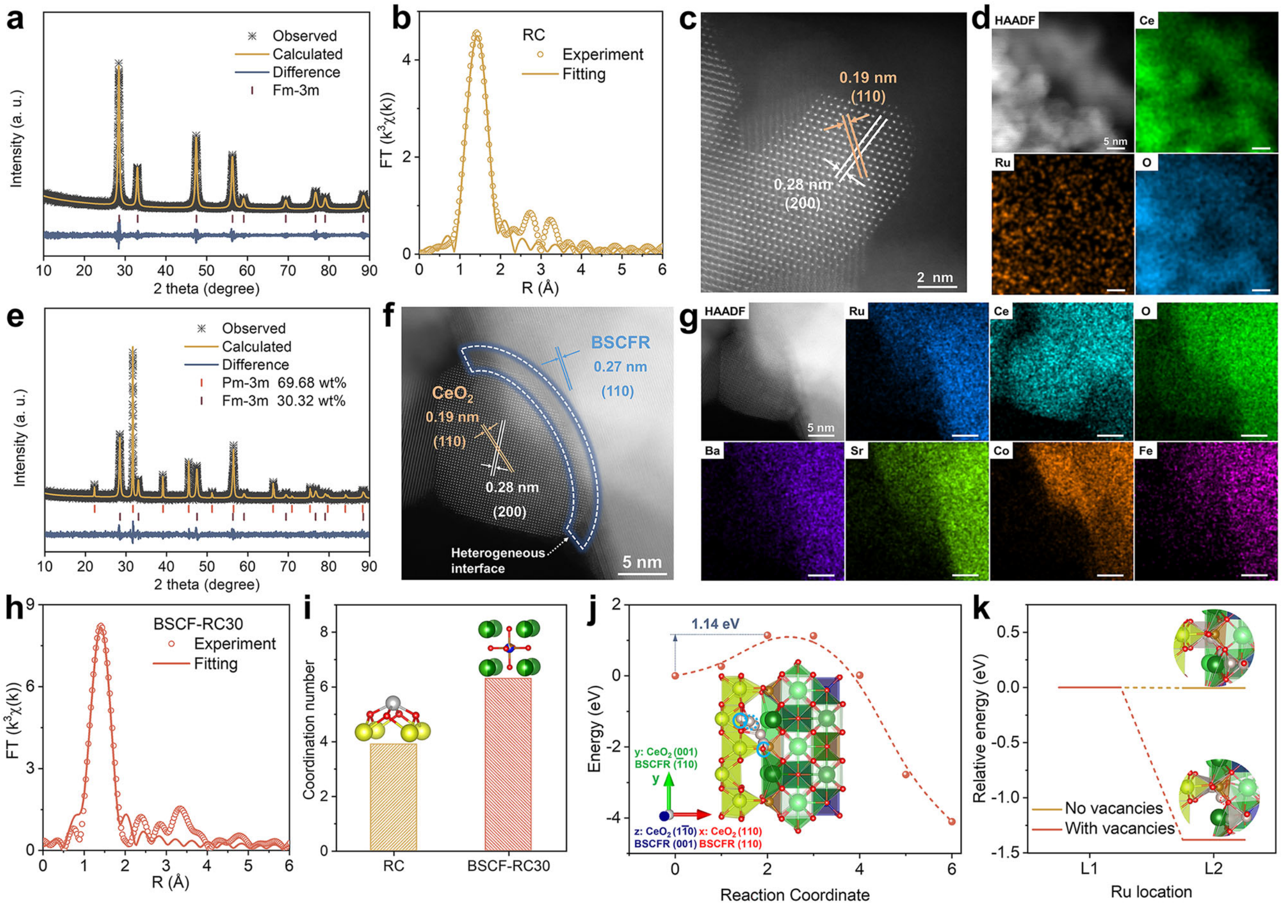

Fig. 2 | Structural and component analysis, and revelation of atom trapping processes. a XRD Rietveld refinement patterns of RC catalyst. **b** Ru K-edge FT-EXAFS spectrum in RC sample. HAADF-STEM image (**c**) and EDS measurements (**d**) for RC catalyst. **e** XRD Rietveld refinement patterns of the hybrid BSCF-RC30. HAADF-STEM (**f**) and EDS mapping (**g**) analyses of the BSCF-RC30. **h** FT Ru K-edge EXAFS spectrum in BSCF-RC30 sample. **i** Average coordination number of Ru ions in RC and BSCF-RC30 catalysts, and the corresponding coordination diagrams are inserted. **j** DFT Calculated energy profile of Ru migration from CeO_2 into BSCF at the BSCF-RC interface, the corresponding migration pathway is inserted. The reactant, transition state, and product are highlighted with blue solid, dotted, and dashed lines, respectively. **k** Thermodynamic energy comparison when the Ru atom is located at the surface (L1) and subsurface layer (L2), with or without oxygen vacancy, the corresponding local model diagrams are inserted. The color code applies to the illustrations in (**i**–**k**): yellow (Ce), red (O), silver (Ru), blue (Co), brown (Fe), dark green (Sr), light green (Ba).

Aberration-corrected STEM and EELS decrypt the spatial charge compensation dynamics underpinning. Atomic-resolution elemental analysis reveals strong chemical bonding between BSCF and RC phases, with Ru species preferentially stabilized at perovskite lattice sites (Supplementary Fig. 17)[7]. Line-scan profiles across the BSCF-RC interface identify two interrelated phenomena (Fig. 3d). First, the penetration of Ru atomic signal into BSCF domains at 2–3 nm (point A: Ru M-edge), accompanied by localized oxygen depletion (O K-edge) at the interface (point B), suggesting that oxygen vacancies are generated at the interface as a result of Ru migration[9,27]. A change in oxygen content is typically associated with variations in the oxidation states of metal ions due to charge transfer. As shown in Fig. 3e, f, EELS spectra of the Co L-edge and Ce M-edge further demonstrate charge transfer at the heterogeneous interface. The Co L-edge shifts to higher energies, indicating an increase in the oxidation state of Co, while the Ce M-edge shifts to lower energies, signifying a reduction in the oxidation state of Ce. The Ce^{4+} characteristic peaks (883 eV) detected at positions E and F adjacent to the bulk RC phase exhibited enhanced intensity compared to those at the interfacial position D, thereby providing additional evidence for the valence state reduction of Ce at the interface[39]. These antiphase electron transfers establish interfacial dipolar fields that stabilize trapped Ru species while lowering the barrier for oxygen exchange, which is key to unlocking bifunctional ORR/OER activity. Furthermore, TEM-EDS mapping of BSCF-RC30 collected after calcination at 600 °C for 200 h still detected Ru only in the BSCF domains (Supplementary Fig. 18). These results verify that atomic trapping arises from the combined thermodynamic driving force for Ru migration and the presence of robust anchoring sites (oxygen vacancies and strong Ru-O-Co/Fe covalent bonds) which lock Ru irreversibly after migration, rather than permitting the random, reversible diffusion expected from a purely chemical-potential-driven process[40].

The oxygen vacancy reservoir directly governs the catalyst's oxygen handling capacity, so we quantified oxygen vacancy differences using thermogravimetric analysis (TGA) and iodine titration (Supplementary Fig. 19). TGA curves acquired in air (50–1000 °C) show that BSCF-RC30 (Ru-trapped composite) exhibits a higher total weight loss (~1.65%) compared to Ru-free BSCF-C30 (~ 1.40%). Since the RC phase itself is thermally stable (negligible mass loss), this additional weight loss in BSCF-RC30 directly reflects enhanced oxygen vacancy formation induced by Ru migration. In addition, O_2 temperature-programmed desorption (O_2-TPD) also verifies that BSCF-RC30 hybrid has a good oxygen dynamic exchange capacity than the BSCF-C30 composite (Supplementary Fig. 20). Iodometric titration shows that the average oxygen non-stoichiometry (δ) of BSCF-RC30 increases by ~28% before and after thermal treatment (Supplementary Fig. 21). This increase is further confirmed by deconvoluted XPS O 1s spectra

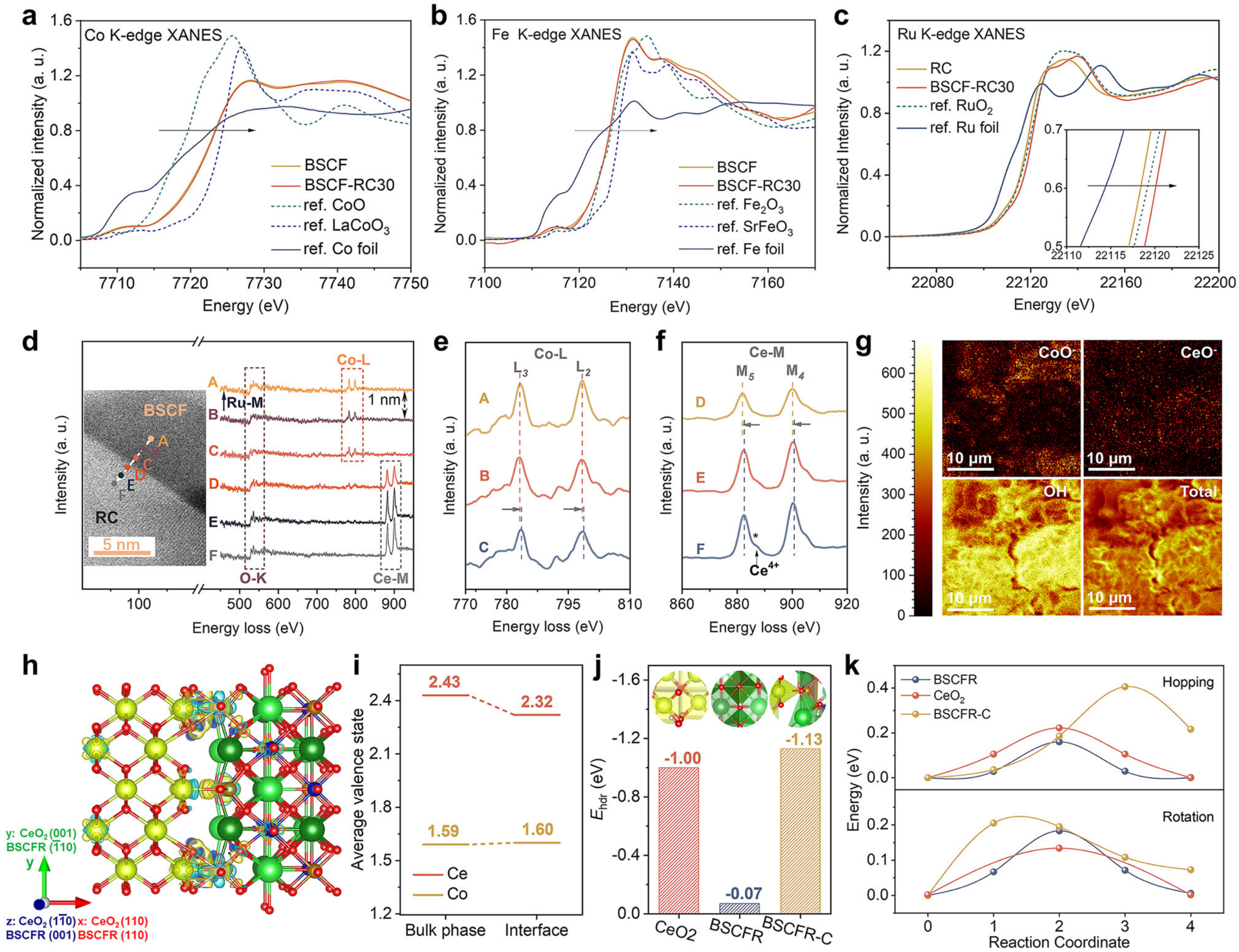

Fig. 3 | Spectroscopic analysis and theoretical calculations. **a**–**c** The XANES spectra at (**a**) Co K-edge, (**b**) Fe K-edge and (**c**) Ru K-edge. The inset shows localized enlargement. **d** Line scanning EELS spectra of the BSCF-RC30 catalyst. The insert displays a STEM plot of the heterogeneous catalyst's localized interface, labeling the locations of the associated data points and the paths of the line scan. **e**, **f** Comparison of EELS spectra about (**e**) Co L-edge and (**f**) Ce M-edge at different sites on the catalyst. **g** Secondary ion mapping images of CeO^-, CoO^-, OH^-, and total species on the surface of heterogeneous catalyst after water treatment. **h** The differential charge density plot of BSCFR-C heterogeneous interface. Electron accumulation and depletion regions are highlighted in yellow and blue, with an isosurface level of 0.005. Atomic color code is the same as that in Fig. 2j. **i** Average valence states of Co and Ce ions at the interface and in the bulk phase. **j** DFT calculated E_{hdr} of the catalysts. The inserts show the hydration sites of the corresponding model. **k** Energy profiles of proton hopping and rotation at BSCFR bulk structure, CeO_2 bulk structure, and BSCFR-C interface. The color code applies to (**h**, **j**): yellow (Ce), red (O), silver (Ru), blue (Co), brown (Fe), dark green (Sr), light green (Ba).

(Supplementary Fig. 22)[41]. The results show that the treated BSCF-RC30 exhibits an increase in the ratio of active oxygen species (O_2^{2-}/O^-) from 32% to 41% compared with the untreated BSCF-RC30, which is consistent with more oxygen vacancies at the heterointerface.

Hydration behavior of the interface, another critical performance determinant in reversible proton-conducting cells. ToF-SIMS analysis (Fig. 3g) reveals the distribution of CeO^-, CoO^-, and OH^- ions in BSCF-RC30 after treatment at 500 °C for 5 h in humidified air (10% H_2O-air)[42]. Notably, the RC phase exhibits a stronger hydration capacity than the BSCF phase, with the interface showing a particularly high concentration of OH^- ions. The enhanced hydration performance at the interface is attributed to the increased oxygen vacancy content, which accelerates the introduction of protons. This selective hydration stems from synergistic contributions: the high surface area of nanoporous CeO_2 domains (63.47 $m^2\ g^{-1}$) provides abundant active sites for the hydration reaction, while the interfacial oxygen vacancies provide the dissociation sites (Supplementary Fig. 23). H_2O-TPD analysis (Supplementary Fig. 24) shows that the RC catalyst displays the strongest H_2O desorption peak compared to both BSCF-RC30 and BSCF oxides, further indicating effective hydration properties. The infrared (IR) spectroscopy (Supplementary Fig. 25) also confirms the presence of prominent hydroxyl signals at 3400 cm^{-1} in the RC and BSCF-RC30 samples, while bulk BSCF regions retain only weak adsorbed water signatures, providing additional evidence of the improved hydration capability of the BSCF-RC30[43].

To further elucidate the activation mechanism and interface effect of the heterogeneous catalyst, we perform DFT calculations based on the experimental data and establish the BSCFR-C heterogeneous interfacial structure. The calculations confirm the strong interfacial coupling formed via charge transfer between Ce atoms in CeO_2 phase and O atoms in BSCFR phase (Fig. 3h). Compared to the valence state in the bulk phases, this interfacial charge redistribution manifests as a coordinated increase in Co oxidation state with concurrent Ce valence drop at the phase boundary (Fig. 3i), establishing an electronic bridge that enhances catalytic functionality. Furthermore, compared to the hydration energy (E_{hdr}) of −1.00 eV and −0.07 eV in CeO_2 and BSCFR bulk structure, BSCFR-C interface represents the minimum E_{hdr} of −1.13 eV (Fig. 3j), which aligns well with the EELS and

ToF-SIMS findings (Fig. 3d–g)[19,26,44]. Proton conduction at heterogeneous interface is also explored (Supplementary Fig. 26). After Ru atom trapping, the proton migration energy of BSCFR (Hopping: 0.16 eV; Rotation: 0.18 eV) is notably lower than the pristine BSCF (Hopping: 0.52 eV; Rotation: 0.29 eV), realizing a low proton migration energy similar to that of CeO_2 (Hopping: 0.22 eV; Rotation: 0.13 eV)[26]. Although the average proton migration barrier at the interface is slightly higher than that of the overall BSCFR and CeO_2, the localized oxygen vacancy channel allows efficient Grothaus-type proton rotation with a migration barrier as low as 0.21 eV, which is close to that of the bulk phase (Fig. 3k and Supplementary Table 3)[45,46].

For electrical conductivity, the BSCF-RC30 heterogeneous catalyst achieves an electrical conductivity of 28.5–38.2 S cm^{-1} at 300–800 °C (Supplementary Fig. 27), which retains the major metal conduction contribution and competitive with reported triple-conducting air electrodes, such as BCFZY (0.4–2.1 S cm^{-1} at 400–800 °C) and $BaCo_{0.7}(Ce_{0.8}Y_{0.2})_{0.3}O_{3-\delta}$ (BCCY) (1.3–4.3 S cm^{-1} at 400–800 °C). This multimodal conduction synergy transforms the engineered interface into a three-phase reaction hotspot, where the ORR and OER processes couple efficiently with proton diffusion, an active property not found in any of the individual components.

Electrochemical activity analysis

To evaluate the electrocatalytic performance of the derived air electrodes in R-PCECs, symmetric cells employing BZCYYb electrolyte were fabricated[47]. Although the single fluorite-structured RC contains atomically dispersed Ru active sites, its insufficient oxygen ion/electronic conductivity hinders charge transport, leading to a very large polarization resistance (R_p) (~2500 Ω cm^2 at 550 °C) when used as a standalone air electrode, which is not sufficient to meet the performance requirements of R-PCECs (Supplementary Fig. 28). BSCF perovskite has high oxygen ion/electron conductivity, abundant oxygen vacancies, and its lattice can stabilize the migration of Ru atoms by forming Ru-O-B (B=Co/Fe) bonds. Upon compositing, BSCF's good conductivity compensates for RC's charge transport limitations, while the interfacial active sites (generated by Ru trapping) synergize with BSCF's oxygen vacancies to enhance oxygen reduction/evolution kinetics. EIS measurements of bare BSCF and BSCF-RCx ($x = 20$, 30, 40 wt%) heterogeneous electrodes were conducted between 500 and 700 °C under dry air conditions. At 600 °C, the ASR of the bare BSCF electrode measures 0.52 Ω cm^2, while BSCF-RC20, BSCF-RC30, and BSCF-RC40 electrodes exhibit reduced ASR values of 0.35, 0.28, and 0.36 Ω cm^2, respectively (Supplementary Fig. 29). This systematic improvement in oxygen reduction reaction activity with RC catalyst incorporation highlights enhanced heterogeneous interfacial kinetics. Among these, the BSCF-RC30 electrode demonstrates optimal performance due to balanced RC content (30 wt%) and interfacial dispersion, maximizing synergistic effects. Under practical operating conditions (5% H_2O-air at 600 °C), the BSCF-RC30 electrode achieved a remarkably low ASR of 0.08 Ω cm^2, outperforming bare BSCF (0.28 Ω cm^2) and other composites (BSCF-RC20: 0.18 Ω cm^2; BSCF-RC40: 0.13 Ω cm^2) (Supplementary Fig. 30). These results confirm that Ru atom trapping simultaneously enhances ORR activity and oxygen activation capability in humid environments. For completeness, we repeated the symmetric-cell test with an independently fabricated specimen (Cell #2). As shown in Supplementary Fig. 31, the resulting ASR values deviate by no more than ±6% from the previous ones over 500-700 °C, confirming that the low-resistance trend is highly reproducible and intrinsic to the atomic-trapping interface. Activation energy analysis derived from ASR-temperature dependence (500-700 °C) reveals values of 1.04, 1.02, 0.94, and 0.96 eV for bare BSCF, BSCF-RC20, BSCF-RC30, and BSCF-RC40 under 5% H_2O-air conditions, respectively (Fig. 4a). The minimized activation energy (0.94 eV) of BSCF-RC30 underscores its enhanced catalytic efficiency and potential for low-temperature applications. The distribution of relaxation time (DRT) as an effective means to analyze the EIS was employed to further explore the electrochemical processes at the air electrode[5,48]. DRT deconvolution identifies three polarization contributions: high-frequency (>10^3 Hz, charge transfer), mid-frequency (10–10^3 Hz, surface ion exchange and bulk ion diffusion), and low-frequency (<10 Hz, surface mass transport) (Fig. 4b). Under 5% H_2O-air at 600 °C, the MF resistance of the bare BSCF electrode is significantly higher than that of the heterogeneous electrodes with Ru atom trapping, indicating that the interfacial effects and synergistic interactions in BSCF-RC30 facilitate improved surface ion exchange and bulk phase diffusion. Furthermore, the BSCF-RC30 electrode exhibits effective surface mass transfer properties compared to other electrodes, further emphasizing the enhanced electrocatalytic performance due to atom trapping.

To confirm the promotion of catalytic activity through Ru atom trapping, additional electrodes were prepared for comparison. These included CeO_2-modified BSCF (BSCF: C = 70: 30 wt%, denoted as BSCF-C30), Ru-doped $Ba_{0.5}Sr_{0.5}(Co_{0.8}Fe_{0.2})_{0.98}Ru_{0.02}O_{3-\delta}$ (BSCFR0.02), and BSCFR0.02-C30 (BSCFR0.02: C = 70: 30 wt%) air electrodes, and their electrochemical performances were tested using symmetric cells at 500 °C with 5% H_2O-air (Supplementary Fig. 32). The corresponding ASRs are 1.22, 1.31, and 1.19 Ω cm^2 for BSCF-C30, BSCFR0.02, and BSCFR0.02-C30, respectively, while the ASRs of BSCF and BSCF-RC30 electrodes are 1.50 and 0.57 Ω cm^2. The BSCF-RC30 electrode exhibits an ASR of only 0.57 Ω cm^2, markedly lower than BSCF-C30 (1.22 Ω cm^2), BSCFR0.02 (1.31 Ω cm^2), and the combined BSCFR0.02-C30 (1.19 Ω cm^2). This pronounced advantage arises from Ru trapping, which establishes a highly active CeO_2/BSCF heterointerface, while the efficient charge transfer and abundant vacancies at the interface not only provide active sites for hydration and oxygen activation, but also promote ion exchange between the two phases, which is an interfacial synergistic effect that neither simple CeO_2 modification nor Ru pre-doping can provide. These results demonstrate that, while Ru doping or CeO_2 composites can enhance BSCF's electrochemical activity, the catalytic performance of simple CeO_2 modification is far less significant than the RC catalyst. The improved performance of BSCF-RC30 is attributed to the trapping of Ru atoms, which not only enhances oxygen activation but also improves hydration and interaction kinetics between phases.

To assess the universality of the improved interfacial effects and catalytic activity, we extended the strategy to other Co-based air electrodes rich in oxygen vacancies, including $PrBaCoO_{5+\delta}$ (PBC), BCFZY, $SrCo_{0.8}Fe_{0.1}Nb_{0.1}O_{3-\delta}$ (SCFN), and $La_{0.6}Sr_{0.4}Co_{0.2}Fe_{0.8}O_{3-\delta}$ (LSCF), known for their marked oxygen activation ability. Indeed, elemental mapping of the as-prepared BCFZY-RC30 composite (Supplementary Fig. 33) likewise shows Ru exclusively anchored on the BCFZY side, confirming that oxygen-vacancy-assisted Ru trapping is both universal and robust across diverse perovskite hosts. EIS tests were performed on symmetric cells for hybrid electrodes compared to pristine counterparts (Supplementary Fig. 34). The ASRs of PBC-RC30, BCFZY-RC30, SCFN-RC30, and LSCF-RC30 electrodes are measured as 2.16, 2.00, 2.45, and 2.3 Ω cm^2, respectively, under dry air conditions at 500 °C. These values show a significant decrease compared to their pristine counterparts, PBC (4.16 Ω cm^2), BCFZY (4.38 Ω cm^2), SCFN (4.90 Ω cm^2), and LSCF (5.16 Ω cm^2), with reductions of 48.1%, 54.3%, 50.0%, and 55.4%, respectively (Fig. 4c), confirming the efficacy of the atom trapping strategy in enhancing ORR activity across various perovskite-based materials wealthy in oxygen vacancies. Further EIS tests under a 5% H_2O-air atmosphere (Supplementary Fig. 35) demonstrate that the catalytic activity of the air electrodes is significantly enhanced, particularly in humid air. For instance, the ASRs of the SCFN electrode are 0.10, 0.23, 0.49, 1.37, and 4.14 Ω cm^2 at 700, 650, 600, 550, and 500 °C, respectively. In contrast, the ASRs of the SCFN-RC30 electrode at the same temperatures are found to be 0.04, 0.09, 0.16, 0.32, and 0.76 Ω cm^2, respectively. This reduction in ASR by 60% at 700 °C and 81.6% at 500 °C further emphasizes the benefits of

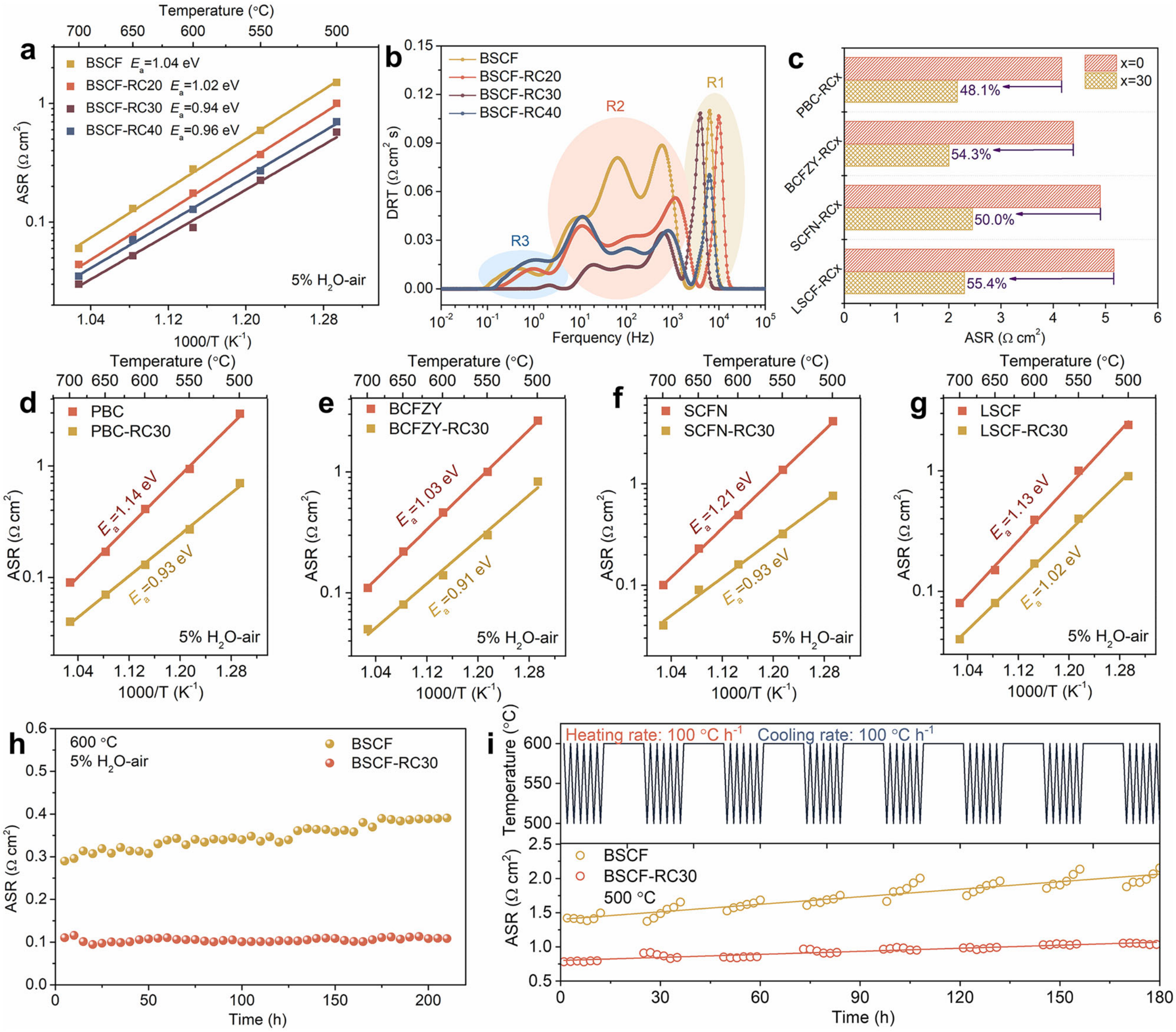

Fig. 4 | Electrochemical activity and thermal stability. **a** Arrhenius plots of the ASRs of the BSCF and BSCF-RC*x* ($x = 20$, 30, and 40 wt%) air electrodes under humidified 5% H_2O-air conditions. **b** DRT analysis of the EIS of the BSCF and BSCF-RC*x* air electrodes at 600 °C. **c** Comparison of ASR values of PBC, BCFZY, SCFN, and LSCF air electrodes with and without the addition of RC catalyst measured at 500 °C in dry air. **d**–**g** Arrhenius plots of the ASRs of the (**d**) PBC, (**e**) BCFZY, (**f**) SCFN and (**g**) LSCF air electrodes and their composite RC catalyst at 500–700 °C. **h** Stability tests of BSCF and BSCF-RC30 air electrodes at 600 °C for 210 h. **i** The ASR response corresponding to 500 °C of symmetric cells with BSCF and BSCF-RC30 air electrodes during 48 thermal cycles between 600 and 500 °C.

incorporating the RC catalyst for enhancing the electrochemical activity of the air electrode in humid conditions. Notably, LN-RC30 electrode shows no performance enhancement due to absent Ru atom trapping, emphasizing the critical role of this mechanism. The ASR of the LN electrode in humid air ranged from 0.18 to 8.10 Ω cm² at 700–500 °C (Supplementary Fig. 36). However, lack of interfacial activity and poor ion transport are the main reasons for the LN-RC30 electrode to exhibit low electrochemical activity under dry and humid air conditions, with ASRs of 0.52 and 0.65 Ω cm² at 600 °C (Supplementary Fig. 37).

As shown in Supplementary Fig. 38, the activation energies of PBC, BCFZY, SCFN, and LSCF air electrodes increase upon mixing with the RC catalyst compared to pristine counterparts under dry air conditions. Interestingly, under 5% H_2O-air conditions, the activation energies of PBC-RC30, BCFZY-RC30, SCFN-RC30, and LSCF-RC30 air electrodes are lower than those of the pristine counterparts (Fig. 4d–g). The observed differences in activation energy patterns under dry and humid air conditions can be attributed to the varying contributions of the perovskite phase and the RC catalyst to the electrochemical reactions on the surface of R-PCECs air electrodes. In dry air, hybrid electrodes exhibit higher activation energies due to limited oxygen vacancy mobility in the RC phase. Conversely, humid conditions enable proton migration through CeO_2-rich interfaces, reducing temperature dependence.

The stability of the electrodes is critical for ensuring long-term performance in R-PCECs. Stability tests on symmetric cells with BSCF and BSCF-RC30 electrodes were conducted in a 5% H_2O-air atmosphere at 600 °C for up to 210 h. As displayed in Fig. 4h, the ASR of the BSCF electrode increases by 34.9% over the test period, with a growth rate of 4.81×10^{-4} Ω cm² h⁻¹. In contrast, the ASR of the BSCF-RC30 electrode shows no significant increase, demonstrating its evident catalytic stability. The stable performance of the BSCF-RC30 electrode is attributed to the formation of a protective layer of CeO_2, which mitigates Ba and Sr segregation upon contact with water vapor (Supplementary Fig. 39). Additionally, CeO_2 exhibits both effective water adsorption and hydration capabilities and effectively mitigates the Ba

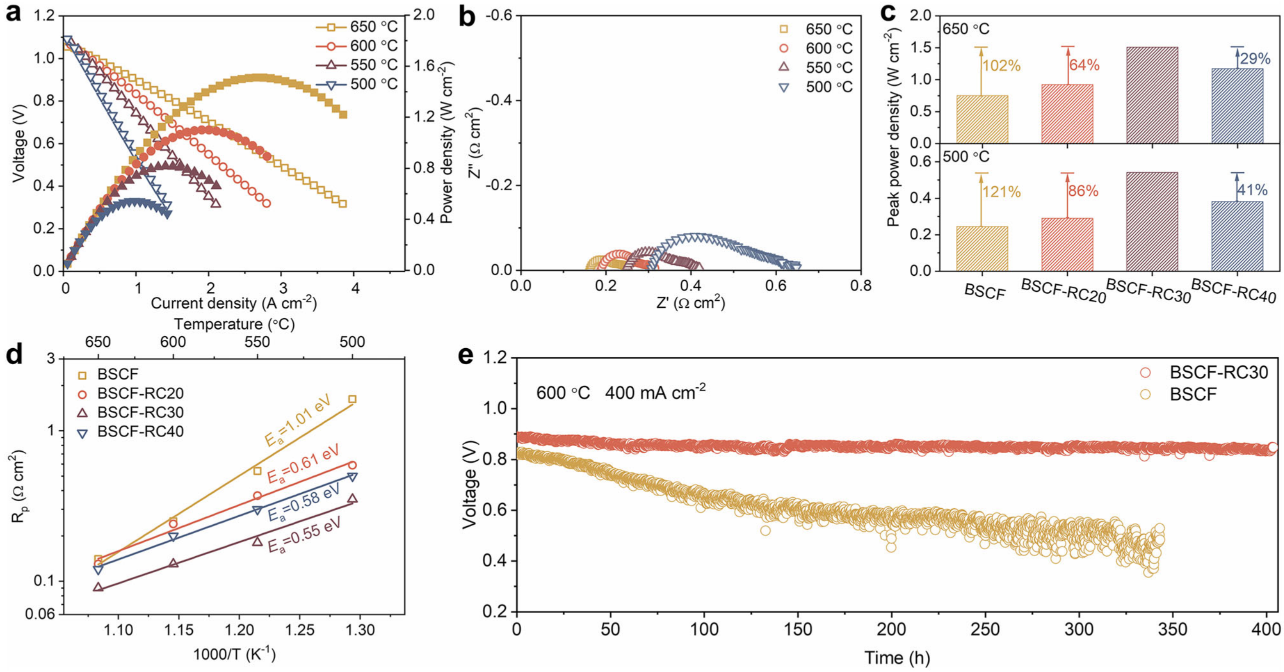

Fig. 5 | Performance and stability of BSCF-RC*x* cells in PCFC mode. **a** Current-voltage polarization and power density curves at different temperatures for the BSCF-RC30 air electrode. **b** Corresponding electrochemical impedance spectra at open circuit voltage. **c** Peak power density comparison for BSCF-RC*x* series cells operated at 650 and 500 °C. **d** Arrhenius plots of R_p for single cells at the test temperatures. **e** Long-term stability testing of cells with BSCF-RC30 and BSCF electrodes at 600 °C in PCFC mode at a constant current density of 400 mA cm^{-2}.

and Sr segregation resulting from the contact of the BSCF phase with water vapor. Not only that, but the BSCF-RC30 electrode behaves similarly stable under dry air (Supplementary Fig. 40). Further stability tests were conducted under severe thermal cycling conditions. As depicted in Fig. 4i and Supplementary Fig. 41, the ASR values of the BSCF-RC30 electrode increase by 0.06 and 0.25 Ω cm^2 at 600 and 500 °C, respectively, over 48 cycles of 180 h. In contrast, the ASR values of the BSCF electrode under the same conditions increase by 0.12 and 0.73 Ω cm^2 at 600 and 500 °C, respectively. The small increase in ASR of the BSCF-RC30 electrode during thermal cycling demonstrated the tolerance of the catalyst. This improved performance is primarily attributed to the BSCF-RC30 electrode's stable phase structure, lower thermal expansion coefficient (TEC), and sustained catalytic activity (Supplementary Fig. 42). XRD patterns show that the BSCF-RC30 hybrid remains pure cubic and fluorite after sintering at 600 °C for 200 h, without the formation of RuO_2 or alkaline earth metal second phases (Supplementary Fig. 43). Complementarily, XPS shows no shift in the Ru 3*p* binding energy, indicating an unchanged oxidation state, while TEM-EDS mapping reveals Ru confined to the BSCF lattice/heterointerface with negligible signal in the CeO_2 domain (Supplementary Fig. 44, 18). The unchanged crystal structure, electronic state, and spatial distribution collectively demonstrate that Ru remains securely anchored, with no detectable segregation or reverse migration during extended operation, underscoring the long-term robustness of the atomic-trapping strategy.

The performance of R-PCECs in PCFC mode

The enhanced heterogeneous interface activity resulting from Ru atom trapping allows the BSCF-RC*x* air electrodes to demonstrate competitive performance in R-PCECs. To evaluate the impact of different composite ratios on the performance of the air electrodes, button cells with the geometry Ni-BZCYYb|BZCYYb|BSCF-RC*x* ($x = 0$, 20, 30, and 40 wt%) were fabricated. Dry hydrogen and humid air were used as the proton and oxygen sources for the fuel electrode and air electrode, respectively (Supplementary Fig. 45). The current-voltage polarization and power density curves for the R-PCECs with BSCF-RC*x* ($x = 0, 20, 30,$ and 40 wt%) electrodes in PCFC mode are presented in Fig. 5a and Supplementary Fig. 46. Among them, the button cell with BSCF-RC30 electrode obtains peak power densities (PPD) of 1.51, 1.10, 0.82, and 0.54 W cm^{-2} at 650, 600, 550, and 500 °C, respectively (Fig. 5a). The single-cell performance was likewise reproduced on a second device prepared under identical conditions. Peak power densities differ by only 2.2% at 650 °C and <3% at 550 °C (Supplementary Fig. 47), underscoring the robustness and reliability of the composite-electrode design. Illustrated in Fig. 5b, the EIS of this cell, measured at open circuit voltage (OCV), shows remarkably low R_p values of 0.09, 0.13, 0.18, and 0.35 Ω cm^2 at 650, 600, 550, and 500 °C, respectively. These findings strongly suggest that the high ORR activity of the air electrode contributes significantly to the performance of this cell. In fuel cell mode on R-PCECs, the performance of the BSCF-RC30 electrode rivals that of recently reported top-tier air electrodes such as $PrNi_{0.5}Co_{0.5}O_{3-\delta}$ (PNC), BCCY, and PBSCF (Supplementary Table 4). Notably, BSCF, BSCF-RC20, BSCF-RC30, and BSCF-RC40 air electrodes exhibit PPDs of 0.75, 0.92, 1.51, and 1.17 W cm^{-2} at 650 °C in PCFC mode, respectively, demonstrating that incorporating RC significantly enhances the performance of BSCF. The addition of RC catalyst, with complex impacts on conductivity, surface mass transfer, ion conduction, and hydration rate of the air electrode, leads to non-linear performance increases as the mass ratio of RC in the electrode rises. At 650 °C, the BSCF-RC30 cell exhibits a performance improvement of over 100% compared to employing a BSCF electrode (Fig. 5c). As the operating temperature decreases, the performance advantage of the BSCF-RC30 cell becomes more apparent, particularly at 500 °C, where it outperforms cells utilizing BSCF, BSCF-RC20, and BSCF-RC40 air electrodes by approximately 121%, 86%, and 41%, respectively.

The EIS analysis of the cells with various air electrodes provides insights into the differences in ORR activity of the BSCF-RC*x* cells at test temperatures (Supplementary Fig. 46). The corresponding R_p to temperature dependence is shown in Fig. 5d. As anticipated, the air electrode BSCF-RC30 demonstrates the lowest activation energy

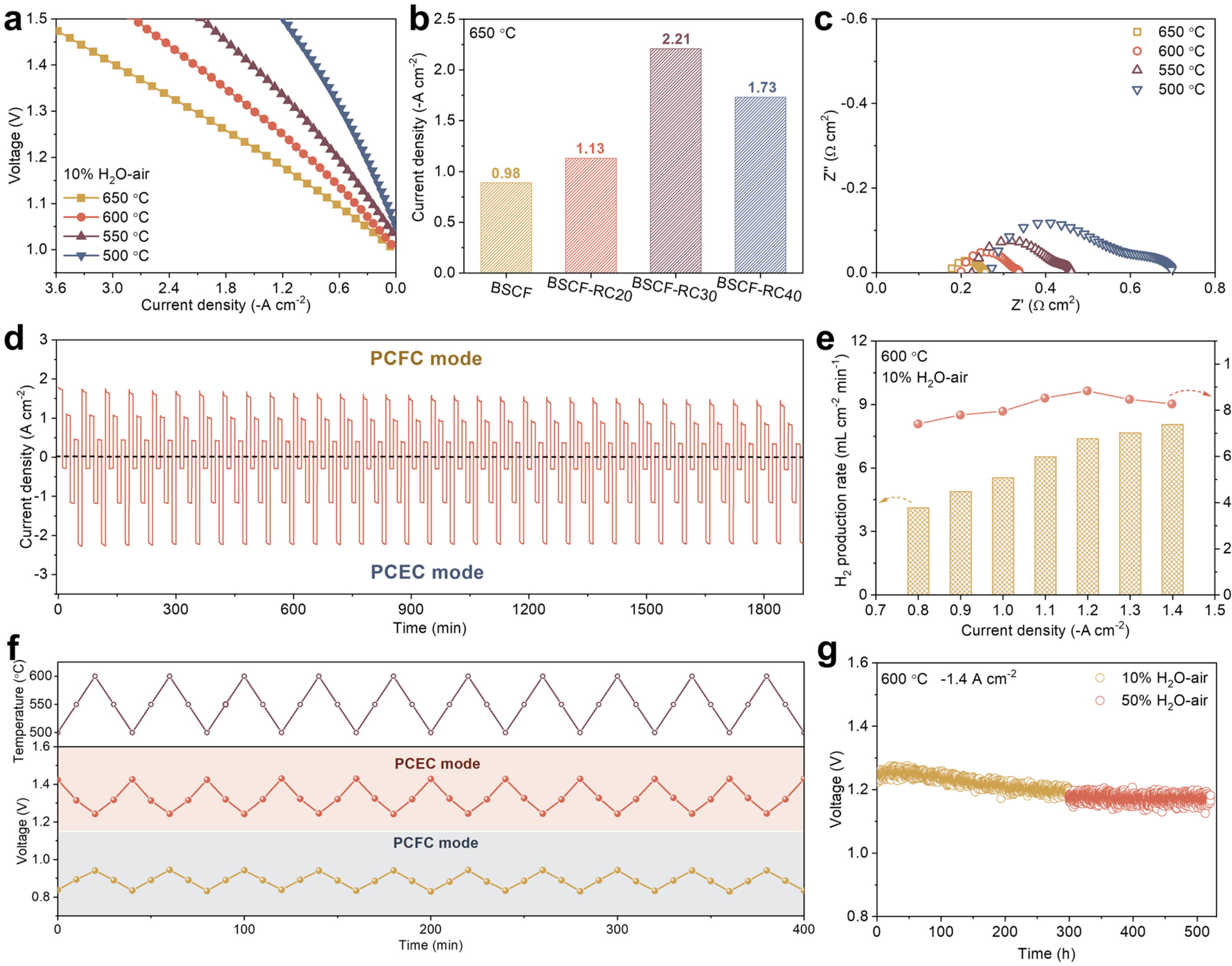

Fig. 6 | Electrochemical performance and tolerability of R-PCECs in PCEC mode. **a** Current-voltage polarization curves for cell made up BSCF-RC30 air electrode at various temperatures with the fuel electrode and air electrode operating in dry H_2 and 10% H_2O-air atmospheres, respectively. **b** Performance comparison of cells using air electrodes with different RC mass ratios at 650 °C in PCEC mode. **c** EIS curve of BSCF-RC30 cell at 1.3 V voltage. **d** The periodic cycling stability of R-PCEC with BSCF-RC30 air electrode in PCFC and PCEC modes, tested for 10 minutes at voltages of 0.8, 1.1, 0.9, 1.2, 1.0 and 1.3 V respectively during each cycle. **e** Hydrogen production rate and FE of electrolytic cells at different current densities at 600 °C. **f** Thermal cycling stability of the cell in PCFC and PCEC modes. **g** Electrolytic stability test of R-PCEC under 10% and 50% H_2O-air conditions.

at 0.55 eV, while the activation energies of BSCF, BSCF-RC20, and BSCF-RC40 are 1.01, 0.61, and 0.58 eV, respectively. These results emphasize that heterogeneous interfaces with abundant active sites and favorable ionic conduction rates can significantly mitigate the temperature dependence of air electrodes, enhancing the potential for R-PCECs at lower operating temperatures. Concerning the electrode stability in fuel cell mode for R-PCECs, Fig. 5e portrays the endurance of the button cell featuring BSCF-RC30 and the bare BSCF electrodes operating at a constant current density of 400 mA cm^{-2} at 600 °C. Over the 350-hour testing period, the voltage of the BSCF cell declines notably from 0.82 to 0.53 V. This decline is primarily attributed to the significant degradation of BSCF electrode performance, induced by extensive Ba and Sr segregation during the prolonged testing period and inadequate thermal compatibility with the BZCYYb electrolyte (Supplementary Fig. 48). In contrast, the cell equipped with the BSCF-RC30 electrode displays no apparent deterioration throughout the 400-hour stability test, affirming the competitive thermochemical robustness of the heterogenous electrode created.

Electrolysis performance and tolerance

R-PCECs featuring varying composite ratios of air electrodes were subjected to testing in PCEC mode, with the air electrode and fuel electrode exposed to 10% H_2O-air and dry H_2, respectively. Figure 6a displays the current-voltage polarization curves of the cell employing BSCF-RC30 as the air electrode. At a voltage of 1.3 V, the cell's current densities reach −2.21, −1.49, −1.07, and −0.58 A cm^{-2} at temperatures of 650, 600, 550, and 500 °C, respectively. Consistent with the electrochemical activity results obtained from symmetric cells testing each electrode independently, the BSCF-RC30 electrode outperforms others in the PCEC mode within the specified temperature range. For instance, at 650 °C, the performances of the BSCF cell, BSCF-RC20 cell, and BSCF-RC40 cell are −0.98, −1.13 and −1.73 A cm^{-2}, respectively. and the BSCF-RC30 cell outperforms them by 125%, 96% and 28%, respectively (Fig. 6b and Supplementary Fig. 49). In addition, the EIS of the cell with the BSCF-RC30 electrode in the PCEC mode is measured at 1.3 V. The resulting R_p values are 0.08, 0.14, 0.24, and 0.43 Ω cm^2 at 650, 600, 550, and 500 °C, respectively, underscoring the high OER activity of the BSCF-RC30 electrode (Fig. 6c). According to our knowledge, the BSCF-RC30 electrode exhibits competitive performance in PCEC mode compared with other reported advanced air electrodes (Supplementary Table 4)[46,49–57].

For R-PCECs, assessing the air electrode's electrocatalytic performance involves conducting stable cyclic operations between PCFC and PCEC modes at various voltages. In this study, we subjected R-PCECs with a BSCF-RC30 electrode to cycling tests at 650 °C, employing voltages in the sequence of 0.8, 1.1, 0.9, 1.2, 1.0, and 1.3 V in both fuel cell and electrolysis cell modes, each for a duration of 10 min. As depicted in Fig. 6d, the cell exhibits consistent and stable performance over 96 cycles, with no noticeable degradation observed in either the fuel cell or electrolysis cell mode. This suggests that the BSCF-RC30 air electrode maintains stable electrocatalytic activity and suitability for application. Additionally, Supplementary Fig. 50 illustrates our examination of the step-like short-term stability of the BSCF-RC30 cell in PCEC mode at 600 °C, revealing competitive stability at voltages of 1.1, 1.2, and 1.3 V.

Faraday efficiency (FE) plays a pivotal role in determining the energy conversion efficiency and economic viability of R-PCECs. However, practical electrolysis processes involve various loss mechanisms, such as electrode reactions, electrolyte ion transport, and impurity reactions, resulting in actual chemical reactant conversion rates falling short of theoretical maxima. The hydrogen production rate and FE of R-PCEC with BSCF-RC30 air electrode were assessed and calculated under the conditions of 600 °C and 10% H_2O-air (Fig. 6e). With an increase in current density from −0.8 to −1.4 A cm^{-2}, the hydrogen production rate rises from 4.12 to 8.06 mL cm^{-2} min^{-1}. Notably, the FE peaks at 88.28% at a current density of −1.2 A cm^{-2}, maintaining around 80% even with further increases in current density. This underscores that a higher FE indicates the potential of R-PCECs for efficient energy conversion, reduced energy consumption, and the promotion of sustainable energy development.

Typically, R-PCECs function within the medium temperature range of 400–650 °C. However, the cyclic variation between high and low temperatures during operation induces continual shifts in internal thermal stress and thermal expansion within the cells. This can lead to issues such as rupture, delamination, or damage, ultimately resulting in degradation or complete failure of the cells. Hence, ensuring robust thermal stability is imperative for extending the lifespan of R-PCECs. Here, we assess thermal stability by monitoring voltage changes in R-PCECs under PCFC (0.4 A cm^{-2}) and PCEC (−0.8 A cm^{-2}) modes during temperature cycling. As demonstrated in Fig. 6f, the cell maintains stable voltage levels through 10 cycles at 500, 550, and 600 °C in both PCFC and PCEC modes. This suggests that the air electrode not only exhibits a stable crystal structure and catalytic activity but also demonstrates competitive compatibility with the electrolyte. Furthermore, the tolerance and long-term stability of R-PCECs under high water pressure were investigated. The cell demonstrates stable operation for 500 h at a current density of −1.4 A cm^{-2} and 600 °C (Fig. 6g). Notably, during the 200-hour test under 50% high water pressure, the cell exhibits stable operation without significant performance degradation. This indicates that the BSCF-RC30 composite air electrode boasts electrochemical stability and tolerance. To elucidate the microscopic origin of this steam tolerance, we next examined whether deleterious surface species develop on the air electrode under humid air conditions. To clarify why the BSCF-RC30 electrode withstands high steam pressures so well, we examined its surface after 24 h in 10% H_2O-air at 600 °C. BSCF-RC30 retains a clean morphology, showing no detectable carbonate or hydroxide deposits, which is attributed to the strong interaction of the heterogeneous interface that inhibits the outward migration of alkaline earth metals from the BSCF bulk phase and the high-surface-area CeO_2 wrapped on the surface to avoid contact with H_2O/CO_2 (Supplementary Fig. 51). In contrast, pristine BSCF forms flaky carbonates after air calcination and densely distributed hydroxide nanoparticles after prolonged wet treatment, which can shorten the triple-phase boundary and slow down proton transfer[58].

Discussion

The dynamic reconstruction of heterogeneous interfaces through thermally activated atomic migration emerges as a paradigm-shifting strategy for achieving stable bifunctional catalysis in proton ceramic electrochemical cells. By harnessing thermodynamic phase equilibria to drive Ru atoms to traverse the fluorite-perovskite interface, we demonstrate a self-optimizing BSCF-RC30 heteroelectrode that fundamentally enhances the interfacial structure and improves interfacial activity. Spectroscopy and DFT calculations reveal that oxygen vacancy-facilitated Ru migration creates covalent metal-oxygen bridges with tailored electron redistribution, establishing fast ion transport networks while enhancing interfacial coupling. Such atom-trapping-based interfacial architecture synergistically maximizes triple conductivity and hydration kinetics, yielding notable performance and stability—PCFC and PCEC modes performance of 1.51 W cm^{-2} and 2.21 A cm^{-2}@1.3 V, respectively, at 650 °C, while stabilizing electrolysis at high water pressure over 500 h. Crucially, the universality of this atomic trapping mechanism is validated across diverse Co-based perovskites rich in oxygen vacancies. This work transcends conventional interface engineering by demonstrating dynamic interfacial self-optimization under operating conditions and providing guidance for the design of next-generation adaptive bifunctional catalytic materials.

Methods

Materials

$Ba(NO_3)_2$, $Sr(NO_3)_2$, $Co(NO_3)_2·6H_2O$, $Fe(NO_3)_3·9H_2O$, $Zr(NO_3)_4·5H_2O$, $Ce(NO_3)_3·6H_2O$, $Gd(NO_3)_3·6H_2O$, $Nb(NO_3)_3$, $La(NO_3)_3·6H_2O$, $Ni(NO_3)_2·6H_2O$, ethylenediaminetetraacetic acid (EDTA), citric acid (CA) monohydrate, isopropyl alcohol, ethylene glycol, glycerol, and ammonia were all analytically pure and purchased from Sinopharm Chemical Reagent Co., Ltd. $Pr(NO_3)_3·6H_2O$, $Y(NO_3)_3·6H_2O$, and $Yb(NO_3)_3·5H_2O$ with a purity of 99.9% were purchased from Shanghai Aladdin Biochemical Co., Ltd. The Ru-based purity of the ruthenium trichloride aqueous solution was 35.0–42.0%, also purchased from Shanghai Aladdin Biochemical Co., Ltd.

Synthesis of catalysts

The powders of BSCF, PBC, LSCF, SCFN, BCFZY, LN, and BZCYYb were all prepared via a citrate-EDTA sol-gel route. All powders/pellets were stored at room temperature under dehumidified conditions (desiccator) until use. In a typical run (illustrated here for BSCF), stoichiometric amounts of $Ba(NO_3)_2$, $Sr(NO_3)_2$, $Co(NO_3)_2·6H_2O$, and $Fe(NO_3)_3·9H_2O$ were first dissolved in deionized water. Separately, citric acid and ethylenediaminetetraacetic acid were co-dissolved in ammonia; this chelating solution was then added to the metal nitrate mixture, and the pH was adjusted to ~7. The overall molar ratio of CA: EDTA: total metal ions was maintained at 2:1:1. Under continuous stirring and gentle heating, the suspension gradually transformed into a clear gel. This gel was dried in an oven at 180 °C to remove residual water, yielding a fluffy precursor powder, which was finally calcined in air at 1000 °C for 5 h to afford the crystalline perovskite oxide. The Ru@$CeO_{2-δ}$ catalyst was obtained by a co-precipitation procedure. $Ce(NO_3)_3·6H_2O$ was dissolved in water at 80 °C, and concentrated ammonia was added dropwise until the solution reached pH ~9, inducing cerium hydroxide precipitation. Then, the corresponding $RuCl_3$ solution was added at a metal atomic ratio of 5% and stirred at 80 °C for 3 h. After cooling to room temperature, the slurry was aged for 12 h, then subjected to three cycles of centrifugation and ultrasonic washing to remove residual chloride. The washed precipitate was dried and finally calcined at 600 °C for 3 h to yield the RC catalyst powder. All composite electrodes were prepared by ball-milling at 400 rpm for 30 min. BSCF and RC were mixed at 80:20, 70:30, and 60:40 (wt%) to obtain BSCF-RC20, BSCF-RC30, and BSCF-RC40, respectively. Likewise, PBC, LSCF, SCFN, BCFZY, and LN were each combined with RC at 70:30 (wt%) to yield M-RC30 composites (M denotes the corresponding oxide). In addition, BSCF and BSCFR0.02 were each combined with CeO_2 at 70:30 (wt%) to produce BSCF-C30 and BSCFR0.02-C30 electrodes.

Cells fabrication

The hydrogen-electrode support was first produced by die-casting a blend of BZCYYb, NiO, and starch (mass ratio 6.5: 3.5: 1). A 0.35 g portion of this powder was then compacted into a 15 mm-diameter disk under 100 MPa via uniaxial pressing. These green pellets were sintered in air at 1000 °C for 2 h to yield the pre-treated support layer. To deposit the BZCYYb electrolyte, 1 g of its powder was dispersed in a mixture of 10 mL ethanol, 2 mL ethylene glycol, and 0.1 g ethylcellulose, and milled at 400 rpm for 60 min. The resulting slurry was drop-cast onto the support by spin-coating at 8000 rpm for 30 s, repeating this cycle three times. The coated half-cells were then fired at 1450 °C for 5 h to form the dense electrolyte. For full-cell assembly, an air-electrode ink was prepared by ball milling the electrode powder with isopropanol, ethylene glycol, and glycerol in a ratio of 1 g: 10 mL: 2 mL: 1 mL. This slurry was sprayed onto the electrolyte side of each half-cell at 150 °C, then calcined at 800 °C for 2 h, giving a functional cell with an air-electrode area of 0.28 cm^2. Symmetric cells were made by die-casting 0.4 g of electrolyte powder containing 1 wt% NiO sintering aid into disks and sintering at 1450 °C for 10 h to obtain dense pellets. The dense pellets were polished, then sprayed with electrode paste and sintered (800 °C, 2 h) to complete a symmetrical configuration with a single-sided air electrode area of 1.06 cm^2. The air electrode loading in both single and symmetric cells after calcination was approximately 20 mg cm^{-2}. Finally, silver wire and silver glue (DAD-87, Shanghai, China) were used as the current collectors and sealant. Data for replicated work have come from parallel experiments using the same electrode preparation method.

Characterizations

X-ray diffraction patterns were collected on a Rigaku Smartlab diffractometer using Cu-Kα radiation (λ = 1.5418 Å), and the diffraction data were refined in TOPAS-4.2 to extract precise lattice constants. F20ST TEM/STEM was employed to observe the microstructure and crystal structure of the samples, and HR-TEM, Mapping and STEM at 200 kV were used to capture images. Structural features of the cells were examined using a Hitachi S-4800 SEM. The size change of the air electrode materials in air was detected by Netzsch 402 C/3/G and TEC were calculated. EELS data were acquired using a Hitachi HT7700 operated at 120 kV. BET and XPS tests were carried out using a Quantachrome Autosorb-iQ3 and a PHI5000 VersaProbe spectrometer, respectively. TGA (Model STA 449 F3, NETZSCH) and O_2-TPD (MS, Hiden, HPR20) were used to measure the mass loss and oxygen volatilization of the dried powder samples. ToF-SIMS (ToF-SIMS 5 iontof), H_2O-TPD (MS, Hiden, HPR20), and IR (IS50 FTIR) were used to analyze the hydration capacity of the samples. Samples were pretreated in a 10% H_2O-air atmosphere at 500 °C for 5 h, followed by natural cooling to room temperature. Spectra were acquired at room temperature in static ambient air using a Fourier-transform IR spectrometer. For the H_2O-TPD test, samples were heated from room temperature to 1000 °C at a rate of 3 °C min^{-1} under flowing nitrogen (N_2, 50 mL min^{-1}). Desorbed water species (H_2O, m/z = 18) were monitored in real time using a mass spectrometer. Finally, XAS were recorded at a soft-X-ray beamline of the Taiwan Synchrotron to investigate local electronic and structural environments.

Electrochemical measurements

EIS was carried out on symmetric cells at open circuit voltage using a voltage amplitude of 10 mV over the frequency range from 10^6 to 0.01 Hz . All measurements used a 100 mL min^{-1} gas flow, and humidity was regulated via a high-pressure constant-current pump (LC100 HPLC). Data were recorded on a Solartron 1287 potentiostat coupled with a 1260 A frequency response analyzer. Single-cell evaluation was performed by sealing the cell in a quartz tube with silver adhesive: the fuel electrode faced the tube's interior (dry H_2 at 80 mL min^{-1}) while the air electrode was exposed to humidified air (10 vol% H_2O, 100 mL min^{-1}). I-V-P and I-V characteristics in both fuel-cell and electrolysis modes were measured using a Keithley 2420 source meter. For EIS in fuel-cell mode, spectra were acquired at OCV between 10^6 and 0.1 Hz with a voltage amplitude of 20 mV; in electrolysis mode, impedance was recorded at 1.3 V from 10^6 down to 0.1 Hz with a voltage amplitude of 100 mV. All impedance data a collected and processed using Zview software. The polarization curves and stability tests in R-PCECs were obtained without iR-correction. For the Faraday efficiency test, a single cell employing the same current collection and sealing method was used. The fuel electrode was exposed to hydrogen during temperature rise and converted to argon when the OCV was stabilized, while the air electrode was constantly exposed to a 10% H_2O-air environment. The cell was tested for FE at a constant current density (between −0.8 and −1.4 A cm^{-2} in gradual increments of −0.1 A cm^{-2}). The gas on the effluent side was analyzed in real time by a GC-9860-5CNJ gas chromatograph equipped with a thermal conductivity detector after 30 min of stabilization after the current was applied. To determine electrical conductivity, 0.8 g of air-electrode powder was uniaxially pressed at 100 MPa into a 15 mm × 5 mm rectangular bar, then sintered in air at 1130 °C for 10 h. Conductivity was measured by the DC four-probe method under flowing air (100 mL min^{-1}) over the temperature range 300–800 °C. Except for the BSCF-RC30 electrode, which was tested in both parallel symmetrical cells and single cells, all other electrochemical tests and comparisons were performed only once.

DFT calculation details

All DFT calculations were performed in Vienna Ab initio Simulation Package (VASP)[59]. Plane-wave pseudopotentials were constructed with the full potential projector augmented wave (PAW) method[60], and the exchange correlation was treated with the generalized gradient approximation (GGA) Perdew-Burke-Ernzerhof (PBE) functional[61], with spin polarization and aspherical contributions both considered. A simplified rotationally invariant approach to DFT + U was also applied[62], with Hubbard U-value of 6.3, 5.3, 3.3, and 5 for Ni, Fe, Co, and Ce, respectively. In total, 4 bulk phases are included in DFT calculation, namely, BSCF, BSCFR, C, and LN. A cutoff energy of 500 eV was used during the geometry optimization. The energy convergence criterion of 10^{-5} eV and the force convergence criterion of 0.02 eV/Å were used for electronic and ionic steps, respectively. The K-mesh was 4 × 4 × 2 for LN and 4 × 4 × 4 for other bulk phases (Supplementary Table 5).

Hydration energy (E_{hdr}) of BSCF and BSCFR are based on the unit cell, while that of C and LN are based on the 2 × 2 × 2 and 2 × 2 × 1 supercells, respectively. The energies of these simulation cells (i.e., unit cells or supercells) were labeled as E_{cell}. For a typical hydration reaction shown in following Eq. (1)[63], E_{hdr} can be obtained with $E_{cell\text{-}H}$, E_{H2O}, E_{O2} denoting the energy of simulation cell with an extra proton, isolated water, and oxygen gas molecule using the following Eq. (2):

$$H_2O + O_o^x + V_o^{\cdot\cdot} = 2OH_o \tag{1}$$

$$E_{hdr} = 2E_{cell-H} + E_{cell} - E_{def} - E_{H2O} \tag{2}$$

Due to the very limited amount of proton, the charge on all simulation cells were kept neutral. The energy barriers of proton migration (i.e., hopping or rotation) were determined by CI-NEB method. All surface slabs and interface structures constructed along the *z*-direction, with a vacuum layer over 15 Å. Before the construction of interface structure, 4-layer surface slabs of C (110), BSCF (110), and LN (103) were first cleaved. After that, BSCF-C interface structure was built based on BSCF (110) surface slab and 2 × 2 supercell of C (110) surface slab, while LN-C interface structure was based on 2 × 1 supercell of LN (103) and 2 × 5 supercell of C (110) surface slab. The K-meshes of 2 × 1 × 1 and 1 × 1 × 1 were used for BSCF-C and LN-C interfaces, respectively, and the corresponding lattice parameters and mismatches were provided (Supplementary Table 6). During the geometry optimization and the following calculation of E_{hdr} and proton transport energy barriers in these interfaces, only atoms in the two interface layers were allowed to move, while atoms in other layers were fixed. Also, loose convergence criteria of 10^{-5} eV and 0.05 eV/Å were used due to the high computational cost of interface structures. Regarding Ru migration across the interface, Ru atom was placed as a 4-coordinated interstitial atom in the side of C and a substitution atom of Co in the BSCF side, respectively. The corresponding two configurations were used as the starting and ending points in the CI-NEB calculation of Ru migration energy barriers.

Data availability

All data generated in this study are provided in the paper and Supplementary Information file. Source data are provided with this paper.

References

1. Tang, W. et al. Sintering protonic zirconate cells with enhanced electrolysis stability and Faradaic efficiency. *Nat. Synth.* **4**, 592–602 (2025).
2. Duan, C., Huang, J., Sullivan, N. & O'Hayre, R. Proton-conducting oxides for energy conversion and storage. *Appl. Phys. Rev.* **7**, 011314 (2020).
3. Bian, W. et al. Revitalizing interface in protonic ceramic cells by acid etch. *Nature* **604**, 479–485 (2022).
4. Wu, Z. et al. A comprehensive review of modeling of solid oxide fuel cells: from large systems to fine electrodes. *Chem. Rev.* **125**, 2184–2268 (2025).
5. Liu, F. et al. Lowering the operating temperature of protonic ceramic electrochemical cells to <450 °C. *Nat. Energy* **8**, 1145–1157 (2023).
6. Papac, M., Stevanovic, V., Zakutayev, A. & O'Hayre, R. Triple ionic-electronic conducting oxides for next-generation electrochemical devices. *Nat. Mater.* **20**, 301–313 (2021).
7. Zhang, B. et al. A strongly coupled Ru–CrO_x cluster–cluster heterostructure for efficient alkaline hydrogen electrocatalysis. *Nat. Catal.* **7**, 441–451 (2024).
8. Wang, J. et al. Tailoring the surface of perovskite through in situ growth of Ru/RuO_2 nanoparticles as robust symmetrical electrodes for reversible solid oxide cells. *Adv. Mater. Interfaces* **7**, 2000828 (2020).
9. Choi, M. et al. Interface engineering to operate reversible protonic ceramic electrochemical cells below 500. C. *Adv. Energy Mater.* **15**, 2400124 (2024).
10. Pei, K. et al. Surface restructuring of a perovskite-type air electrode for reversible protonic ceramic electrochemical cells. *Nat. Commun.* **13**, 2207 (2022).
11. Liu, Z. et al. Synergistic dual-phase air electrode enables high and durable performance of reversible proton ceramic electrochemical cells. *Nat. Commun.* **15**, 472 (2024).
12. Shao, Z. P. & Haile, S. M. A high-performance cathode for the next generation of solid-oxide fuel cells. *Nature* **431**, 170–173 (2004).
13. Choi, S. et al. Exceptional power density and stability at intermediate temperatures in protonic ceramic fuel cells. *Nat. Energy* **3**, 202–210 (2018).
14. Wang, Z. et al. Rational design of perovskite ferrites as high-performance proton-conducting fuel cell cathodes. *Nat. Catal.* **5**, 777–787 (2022).
15. Zhu, F. et al. Steam-promoted symmetry optimizations of perovskite electrodes for protonic ceramic cells. *Energy Environ. Sci.* **17**, 7782–7791 (2024).
16. Zhao, C. et al. Heterointerface engineering for enhancing the electrochemical performance of solid oxide cells. *Energy Environ. Sci.* **13**, 53–85 (2020).
17. Zhou, T. et al. Significantly enhanced performance of protonic ceramic fuel cells by laser engineering the electrolyte/cathode interface. *ACS Energy Lett.* **9**, 4557–4563 (2024).
18. Chen, X. et al. Synergistic bulk and surface engineering for expeditious and durable reversible protonic ceramic electrochemical cells air electrode. *Adv. Mater.* **36**, 2403998 (2024).
19. Park, K. et al. Water-mediated exsolution of nanoparticles in alkali metal-doped perovskite structured triple-conducting oxygen electrocatalysts for reversible cells. *Energy Environ. Sci.* **17**, 1175–1188 (2024).
20. Pan, J. et al. Improving the activity and stability of Ni-based electrodes for solid oxide cells through surface engineering: Recent progress and future perspectives. *Mater. Rep. Energy* **1**, 100025 (2021).
21. Yoo, H. S. et al. Interface engineering to improve electrochemical performance of intermediate-temperature solid oxide fuel cells. *Appl. Surf. Sci.* **639**, 158188 (2023).
22. Yan, H., Zhang, N. & Wang, D. Highly efficient CeO_2-supported noble-metal catalysts: From single atoms to nanoclusters. *Chem. Catal.* **2**, 1594–1623 (2022).
23. Sibei, Z. et al. Manufacturing single-atom alloy catalysts for selective CO_2 hydrogenation via refinement of isolated-alloy-islands. *Angew. Chem. Int. Ed.* **64**, e202412835 (2024).
24. Filippova, A. D. et al. Peroxidase-like activity of CeO_2 nanozymes: particle size and chemical environment matter. *Molecules* **28**, 3811 (2023).
25. Bertella, F. et al. Insights into the promotion with Ru of Co/TiO_2 fischer–tropsch catalysts: an in situ spectroscopic study. *ACS Catal.* **10**, 6042–6057 (2020).
26. Liu, Z. et al. Highly active nanocomposite air electrode with fast proton diffusion channels via er doping-induced phase separation for reversible proton ceramic electrochemical cells. *Adv. Funct. Mater.* **34**, 2311140 (2023).
27. Xing, Y. et al. Proton shuttles in CeO_2/$CeO_{2-\delta}$ core-shell structure. *ACS Energy Lett.* **4**, 2601–2607 (2019).
28. Yang, M. et al. Self-optimized and stable nanocomposites via one-pot synthesis for high-temperature CO_2 electrolysis in solid oxide electrolysis cells. *J. Power Sources* **602**, 234277 (2024).
29. Zhuang, Z. et al. Reversely trapping atoms from a perovskite surface for high-performance and durable fuel cell cathodes. *Nat. Catal.* **5**, 300–310 (2022).
30. Song, Y. et al. Surface activation by single ru atoms for enhanced high-temperature CO_2 electrolysis. *Angew. Chem. Int. Ed.* **63**, e202313361 (2023).
31. Zhang, K. et al. Selective hydrodeoxygenation of aromatics to cyclohexanols over Ru single atoms supported on CeO2. *J. Am. Chem. Soc.* **144**, 20834–20846 (2022).
32. Zhai, S. et al. A combined ionic Lewis acid descriptor and machine-learning approach to prediction of efficient oxygen reduction electrodes for ceramic fuel cells. *Nat. Energy* **7**, 866–875 (2022).
33. Yoo, J. S., Rong, X., Liu, Y. & Kolpak, A. M. Role of lattice oxygen participation in understanding trends in the oxygen evolution reaction on perovskites. *ACS Catal.* **8**, 4628–4636 (2018).
34. Tarutin, A. P. et al. Barium-doped nickelates $Nd_{2-x}Ba_xNiO_{4+\delta}$ as promising electrode materials for protonic ceramic electrochemical cells. *Ceram. Int.* **46**, 24355–24364 (2020).
35. Saqib, M. et al. Transition from perovskite to misfit-layered structure materials: a highly oxygen deficient and stable oxygen electrode catalyst. *Energy Environ. Sci.* **14**, 2472–2484 (2021).
36. Lin, X. et al. Machine learning-assisted dual-atom sites design with interpretable descriptors unifying electrocatalytic reactions. *Nat. Commun.* **15**, 8169 (2024).
37. Huang, Q. et al. Activating lattice oxygen by a defect-engineered Fe_2O_3–CeO_2 nano-heterojunction for efficient electrochemical water oxidation. *Energy Environ. Sci.* **17**, 5260–5272 (2024).

38. Guo, Y. et al. In situ exsolved CoFe alloy nanoparticles for stable anodic methane reforming in solid oxide electrolysis cells. *Joule* **8**, 2016–2032 (2024).
39. Xing, Y. et al. Proton shuttles in $CeO_2/CeO_{2-\delta}$ core–shell structure. *ACS Energy Lett.* **4**, 2601–2607 (2019).
40. Zhu, Y. et al. Beyond conventional structures: emerging complex metal oxides for efficient oxygen and hydrogen electrocatalysis. *Chem. Soc. Rev.* **54**, 1027–1092 (2025).
41. Kim, D. et al. On the role of bimetal-doped $BaCoO_{3-\delta}$ perovskites as highly active oxygen electrodes of protonic ceramic electrochemical cells. *Adv. Energy Mater.* **14**, 2304059 (2024).
42. Luo, Z. et al. First observation of electrode-correlated protonic conductivity of perovskite-type electrolytes and way towards optimization. *Energy Environ. Sci.* **17**, 4115–4125 (2024).
43. Xu, Y. et al. A low-lewis-acid-strength cation Cs^+-doped double perovskite for fast and durable oxygen reduction/evolutions on protonic ceramic cells. *ACS Energy Lett.* **8**, 4145–4155 (2023).
44. Fu, M. et al. Sn-doped cobalt containing perovskite as the air electrode for highly active and durable reversible protonic ceramic electrochemical cells. *J. Adv. Ceram.* **13**, 63–72 (2024).
45. Nie, H. et al. Recent advances and challenges in perovskite-based protonic ceramic electrolytes: design strategies and fabrication innovations. *Adv. Funct. Mater.* **35**, 2416651 (2025).
46. Ding, H. et al. Self-sustainable protonic ceramic electrochemical cells using a triple conducting electrode for hydrogen and power production. *Nat. Commun.* **11**, 1970 (2020).
47. Kim, J. H. et al. An universal oxygen electrode for reversible solid oxide electrochemical cells at reduced temperatures. *Energy Environ. Sci.* **16**, 3803–3814 (2023).
48. Liu, Y., Shao, Z., Mori, T. & Jiang, S. P. Development of nickel based cermet anode materials in solid oxide fuel cells - Now and future. *Mater. Rep. Energy* **1**, 100003 (2021).
49. Tang, W. et al. Understanding of A-site deficiency in layered perovskites: promotion of dual reaction kinetics for water oxidation and oxygen reduction in protonic ceramic electrochemical cells. *J. Mater. Chem. A* **8**, 14600–14608 (2020).
50. Shin, J.-S. et al. Activity of layered swedenborgite structured $Y_{0.8}Er_{0.2}BaCo_{3.2}Ga_{0.8}O_{7+\delta}$ for oxygen electrode reactions in at intermediate temperature reversible ceramic cells. *J. Mater. Chem. A* **9**, 607–621 (2021).
51. Liu, Z. et al. One-pot derived thermodynamically quasi-stable triple conducting nanocomposite as robust bifunctional air electrode for reversible protonic ceramic cells. *Appl. Catal. B Environ.* **319**, 121929 (2022).
52. Liang, M. et al. Magnesium tuned triple conductivity and bifunctionality of $BaCo_{0.4}Fe_{0.4}Zr_{0.1}Y_{0.1}O_{3-\delta}$ perovskite towards reversible protonic ceramic electrochemical cells. *Appl. Catal. B Environ.* **318**, 121868 (2022).
53. Song, Y. et al. Nanocomposites: a new opportunity for developing highly active and durable bifunctional air electrodes for reversible protonic ceramic cells. *Adv. Energy Mater.* **11**, 2101899 (2021).
54. He, F. et al. Catalytic self-assembled air electrode for highly active and durable reversible protonic ceramic electrochemical cells. *Adv. Funct. Mater.* **32**, 2206756 (2022).
55. Kim, J. et al. Hybrid-solid oxide electrolysis cell: A new strategy for efficient hydrogen production. *Nano Energy* **44**, 121–126 (2018).
56. Huan, D. et al. New, efficient, and reliable air electrode material for proton-conducting reversible solid oxide cells. *ACS Appl. Mater. Interfaces* **10**, 1761–1770 (2018).
57. Li, W. et al. High performing triple-conductive Pr2NiO4+δ anode for proton-conducting steam solid oxide electrolysis cell. *J. Mater. Chem. A* **6**, 18057–18066 (2018).
58. Shi, N., Xie, Y., Tadé, M. O. & Shao, Z. Evolution and reconstruction of air-electrode surface composition in reversible protonic ceramic cells: mechanisms, impacts on catalytic performance, and optimization strategies-A review. *Adv. Mater.* **37**, 2416528 (2025).
59. Kresse, G. & Furthmüller, J. Efficiency of ab-initio total energy calculations for metals and semiconductors using a plane-wave basis set. *Comput. Mater. Sci.* **6**, 15–50 (1996).
60. Blöchl, P. E. Projector augmented-wave method. *PhRvB* **50**, 17953–17979 (1994).
61. Perdew, J. P., Burke, K. & Ernzerhof, M. Generalized Gradient Approximation Made Simple. *Phys. Rev. Lett.* **77**, 3865–3868 (1996).
62. Dudarev, S. L., Botton, G. A., Savrasov, S. Y., Humphreys, C. J. & Sutton, A. P. Electron-energy-loss spectra and the structural stability of nickel oxide: An LSDA+U study. *PhRvB* **57**, 1505–1509 (1998).
63. Dawson, J. A., Miller, J. A. & Tanaka, I. First-Principles Insight into the Hydration Ability and Proton Conduction of the Solid State Proton Conductor, Y and Sn Co-Doped $BaZrO_3$. *Chem. Mater.* **27**, 901–908 (2015).

Acknowledgements

The work was supported by the National Key R&D Program of China (2022YFB4004000 (G.M.Y.)), the National Natural Science Foundation of China (U24A20542 (G.M.Y.), 52472210 (G.M.Y.), 52302183(R.X.Q.), 22209072 (Y.L.Z.) and 22479075 (Y.L.Z.)), the Natural Science Foundation of Jiangsu Province (BK20221312 (G.M.Y.), BK20230896(R.X.Q.), BK20220879 (Y.L.Z.) and BK20230894 (Y.L.Z.)), the Cultivation Program for the Excellent Doctoral Dissertation of Nanjing Tech University (2023-09 (Z.Q.L.)), and Jiangsu Specially-Appointed Professors (Y.L.Z.). The authors acknowledge the support from the Max Planck-POSTECH-Hsinchu Center for Complex Phase Materials.

Author contributions

Z.Q.L., G.M.Y., and Z.P.S. performed the conceptual design. Z.Q.L., H.S.D., and Y.S.B. conducted material synthesis, electrochemical testing, and data analysis. D.L.L. performed the XRD refinement. Y.X.L. constructed the models and carried out the theoretical analysis. R.X.Q. and D.S.F. acquired S/TEM-EDS and EELS data. J.Z., W.H.H., M.H.Y., C.W.P., and Z.W.H. performed XAS measurements and data analysis. R.R., W.Z., G.M.Y., and Y.L.Z. provided guidance on data interpretation for the manuscript. Z.Q.L., N.S., Z.X.L., G.M.Y., Y.L.Z., and Z.P.S. jointly participated in writing and revising the paper.

Competing interests

The authors declare no competing interests.

Additional information

Supplementary information The online version contains supplementary material available at https://doi.org/10.1038/s41467-025-65386-8.

Correspondence and requests for materials should be addressed to Guangming Yang, Yuxiao Lin or Zongping Shao.

Peer review information *Nature Communications* thanks Hanping Ding and the other, anonymous, reviewer(s) for their contribution to the peer review of this work. A peer review file is available.